RSC Advances

PAPER

View Article Online
View Journal | View Issue

Cite this: *RSC Adv.*, 2026, **16**, 4602

Sustainable magnesium doped nanofibrillated cellulose/bentonite composite for enhanced phosphate removal: process optimization and mechanistic insights

Archana Pandey,[a] Ajay S. Kalamdhad[b] and Yogesh Chandra Sharma *[a]

Excessive accumulation of phosphate anions in aquatic systems accelerates ecological degradation and threatens both environmental quality and public health. In this study, we developed magnesium-doped nanofibrillated cellulose/bentonite (Mg@NFC/BN) composite through a facile *in situ* modification, yielding a cellulose–clay hybrid with enhanced anion affinity. The optimized composite exhibited maximum phosphate adsorption capacity of 19.2 mg g^{-1} and removal efficiency of 88.6%. The adsorption process attained equilibrium within 90 min, following pseudo-second-order kinetics and conforming to Langmuir isotherm behaviour, while thermodynamic analysis indicated a spontaneous and exothermic mechanism. The synthesized adsorbent remained effective across a wide pH range, with strong selectivity even in the presence of competing anions. Structural and surface analyses through point of zero charge (pH_{PZC}), XRD, FTIR, FESEM, EDX and XPS confirmed the successful synthesis of composite and incorporation of Mg, which strengthened electrostatic interactions and promoted inner-sphere ligand exchange with phosphate ions. Alkaline-assisted desorption enabled up to 90% phosphate release, and the adsorbent retained over 75% of its initial capacity even after seven cycles, demonstrating excellent stability and recyclability for nutrient recovery. Beyond water treatment, the phosphate-laden composites improved soil water retention, highlighting their potential for sustainable agricultural applications. Overall, this work expands the functional versatility of cellulose–clay composites, offering an environmentally benign strategy for integrated wastewater remediation and resource recovery.

Received 8th November 2025
Accepted 15th January 2026

DOI: 10.1039/d5ra08609d

rsc.li/rsc-advances

1 Introduction

Elevated inputs of phosphorus (P) from agricultural runoff and wastewater discharge into aquatic ecosystems pose a persistent threat to biogeochemical processes, contributing to ecological degradation and significant threat to water quality.[1] A high concentration of P accelerates eutrophication, leading to redundant growth of algae, hypoxia and creation of dead zones in aquatic environments.[2] While N can often be mitigated through natural biogeochemical pathways such as denitrification, the removal of P from aquatic environments is considerably complex due to its limited mobility and strong binding affinity to sediments.[3] Moreover, global phosphate reserves are projected to deplete within the next 150 years.[4] Therefore, effective phosphate management strategies are critically important for protecting aquatic ecosystems and ensuring resource sustainability.[5]

In recent decades, various strategies have been investigated for P control in aquatic systems, including biological treatments, membrane technology, advanced oxidation processes, chemical precipitation, adsorption, and ion exchange processes.[3,4] However, the practical application of conventional adsorbents is often limited by high synthesis and regeneration costs, post-use disposal challenges, and environmentally burdensome life-cycle characteristics.[6,7] Consequently, recent research efforts have increasingly focused on the development of low-cost and sustainable adsorbents derived from agricultural residues, industrial by-products, mineral clays, and engineered materials for efficient phosphate removal.

Over the past decade, nanofibrillated cellulose (NFC) has gained considerable attention in wastewater treatment systems, owing to its favourable properties such as high specific surface area, biocompatibility, biodegradability, and ease of surface modification through its abundant hydroxy groups.[8,9] These characteristics make NFC a promising candidate as an adsorbent or supporting matrix in contaminant removal *via* adsorption. However, pristine NFC exhibits low affinity for phosphate anions owing to the predominance of hydroxy (–OH) groups on its surface. In addition, the adsorption kinetics of unmodified

[a]*Department of Chemistry, Indian Institute of Technology (BHU) Varanasi, Varanasi 221005, India. E-mail: ysharma.apc@iitbhu.ac.in*
[b]*Department of Civil Engineering, Indian Institute of Technology Guwahati, Guwahati 781039, India*

NFC are relatively slow resulting from their dense and non-porous structure, thus restricting ion diffusion.[10,11] These limitations warrant the development of various NFC modification strategies such as metal oxide loading, polymer grafting, clay based composite preparation, and surface modification, which significantly enhance adsorption capacity of the functionalized NFC and its selectivity toward phosphate.[12]

Bentonite (BN) is a naturally occurring, abundantly available mineral clay that is widely studied as adsorbent either in its natural phase or in its modified forms. As a smectite rich mineral, bentonite exhibits large specific surface area, high surface reactivity, and excellent ion exchange capacity, contributing to its strong adsorption performance.[13,14] In addition, bentonite is characterized by its non-toxicity and biocompatibility, making it environmentally safe for water treatment applications. In this regard, many researchers claimed that incorporating BN into NFC matrices can improve their adsorption capacity due to the synergistic effect of organic–inorganic hybrid composite.[15]

While NFC provides extensive surface area and hydroxyl-rich functionality and BN offers high ion-exchange capacity, their phosphate adsorption performance still remains limited by intrinsic physicochemical constraints. In NFC/BN composite, phosphate uptake is dominated by weak electrostatic interactions and hydrogen bonding, which are easily disrupted in the presence of competing anions such as nitrate, sulphate, and carbonate. Furthermore, under neutral to alkaline conditions, both NFC and BN surfaces become negatively charged, leading to electrostatic repulsion with anionic phosphate species ($H_2PO_4^-$, HPO_4^{2-}). To bridge this gap, this study proposes surface modification of NFC/BN hybrid composite with multivalent metals ion, as a promising and cost-effective approach to enhance the phosphate adsorption affinity of the adsorbent. Among various candidates, divalent cation magnesium (Mg^{2+}) is of particular interest due to its strong binding affinity toward phosphate and its ability to form inner-sphere complexes.[16] Furthermore, the abundant hydroxyl groups of both NFC and BN enable effective coordination with Mg ions ensuring its uniform dispersion through-out the composite matrix. This interaction facilitates NFC intercalation within BN layers, clay exfoliation and increase in basal spacing.[17] As a result, there is a higher density of exposed active sites, improved surface functionality, and an increased point of zero charge (pH_{PZC}), favouring phosphate removal across a wider pH range.[18]

Despite these advantages, Mg-doped NFC/BN composites have not yet been investigated for phosphate removal from wastewater, nor have their underlying adsorption mechanisms been systematically studied. The aim of our investigation are; (i) prepare and optimize Mg doped NFC/BN composite as adsorbent; (ii) verify the physico-chemical properties of composite using XRD (X-ray diffraction), FE-SEM (Field Emission-Scanning Electron Microscopy), EDX (Energy Dispersive X-ray analysis), FTIR (Fourier Transform Infra-red Spectroscopy), pH_{PZC} (point of zero charge) analysis and XPS (X-ray Photoelectron Spectroscopy); (iii) evaluate the phosphate removal performance of adsorbent using batch uptake experiments and experiments with interfering anions; (iv) explore the mechanisms underlying phosphate removal by the adsorbent, assess the stability of the adsorbent and its practical applicability through desorption cycles and (v) assess the water retention property of phosphate laden adsorbent to be re-used in agricultural systems.

2 Experimental

2.1 Materials

All the reagents including raw bentonite used were supplied by SRL Pvt. Ltd and were of analytical grade. Deionized water was utilized in all experiments unless stated otherwise.

2.2 Preparation of adsorbent

NFC was extracted from sugarcane bagasse using the method reported in our previous study.[19] A series of NFC/BN composite adsorbents were prepared by mixing varying mass ratios of NFC and BN (provided in SI file) in a beaker containing 100 mL of distilled water for 12 h. It was then filtered and dried at 90 °C for further use. The composites were designated with subscripts corresponding to their mass ratios.

Following the pre-screening experiments, the composite demonstrating the highest removal efficiency was selected and subsequently subjected to *in situ* mixing with 100 mL of 1.5 M $MgCl_2 \cdot 6H_2O$ solution in the presence of the NFC/BN composite. The prepared mixture was ultrasonicated for approximately 15 min at ambient temperature to obtain better dispersion and homogeneity. Thereafter, 1 M NaOH solution was gradually added to the mixture until the pH reached 10 while vigorously stirring at room temperature for a duration of 6 h. The purpose of alkali treatment in the aforementioned step was to coat magnesium ions onto the NFC/BN composite surface. Following this, the mixture was aged at room temperature for 24 h, filtered and washed repeatedly with distilled water to eliminate any traces of chloride ions. The fractions were dried overnight at 90 °C, gently ground, and passed through a 0.15 mm mesh to obtain a fine powder consistency. Fig. 1 illustrates the schematic representation of adsorbent synthesized using NFC, BN and $MgCl_2$. The obtained composite was labelled as Mg@NFC/BN for understanding.

2.3 Analytical methods

The microstructure and elemental composition were assessed through scanning electron microscopy (SEM) (Nova Nano SEM 450), in conjunction with energy dispersive X-ray spectroscopy (EDX) (Team Pegasus Integrated EDS-EBSD with Octane Plus and Hikari Pro EDAX Inc.). X-ray diffraction (XRD) patterns were obtained using Rigaku Miniflex 600, spanning a range of 5° to 90° 2θ. Fourier transform infrared (FTIR) spectroscopy was employed to analyse the surface functional group characteristics of the absorbent, operated using KBr pellets in the range from 4000 to 400 cm^{-1} (Nicolet iS5, THERMO Electron Scientific Instruments). The pH_{PZC} value for the adsorbent was determined using the pH drift technique.[20] The surface chemical states of the elements involved were analysed by X-ray photoelectron spectroscopy (XPS, K-Alpha Thermo Fisher Scientific).

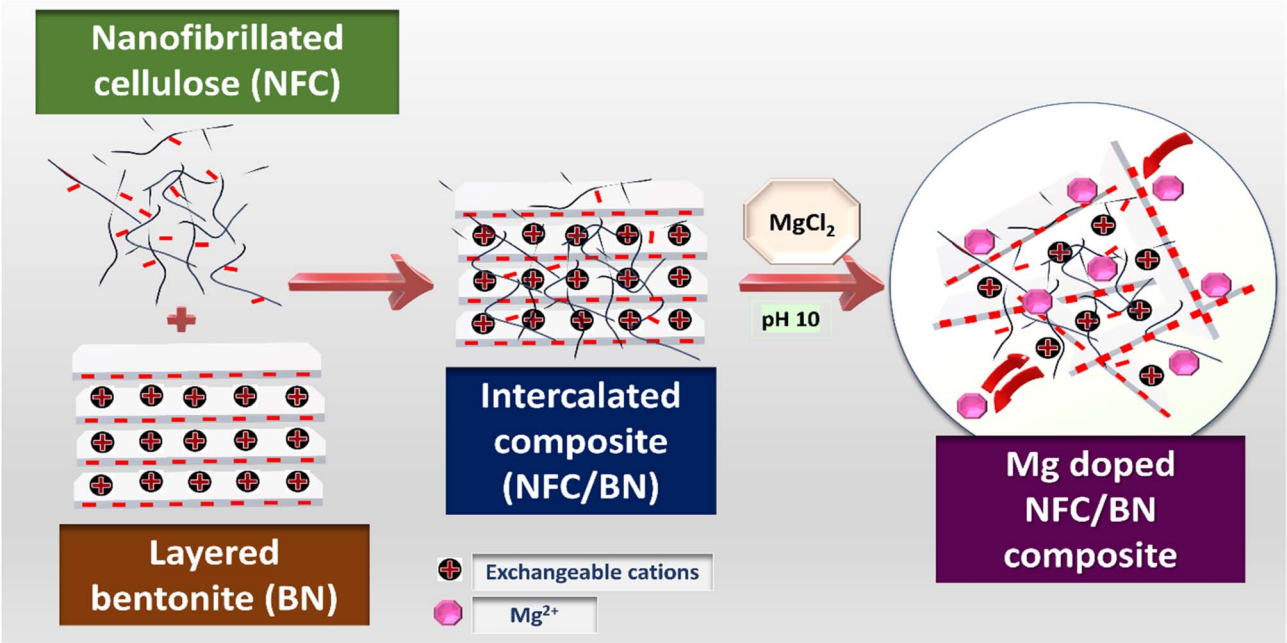

Fig. 1 Schematic diagram depicting the fabrication process of Mg doped NFC/BN.

2.4 Batch adsorption experiments

Potassium dihydrogen phosphate (KH_2PO_4) was dissolved in distilled water to prepare standard solutions for phosphate. A set of batch experiments were conducted to investigate equilibrium isotherm, kinetics rate and thermodynamic studies of phosphate adsorption onto Mg@NFC/BN composite. Comprehensive descriptions of these studies are provided in SI file. The effects of adsorbent dose and solution pH of the adsorbent were determined to assess the efficiency of Mg@NFC/BN. Here, 0.05 g of the adsorbent was mixed in 50 mL solution containing $H_2PO_4^-$ ions and subjected to shaking at 150 rpm at ambient temperature for 1 h. An initial phosphate concentration of 20 mg L^{-1}, representing typical levels in municipal wastewater, was used for all experiments. The initial pH for each system was adjusted to 7 ± 0.02 with 0.01 M of NaOH and HCl prior to the adsorption experiments excluding those performed for pH optimization. The pH values of solutions before and after phosphate adsorption were measured with a pH meter (Thermo Scientific Orion Star A211 pH meter). To evaluate the phosphate adsorption performance of Mg@NFC/BN in complex solutions containing interfering anions (Cl^-, SO_4^{2-}, NO_3^-, HCO_3^-, and F^-) at different molar ratios, batch experiments were conducted with their respective sodium salts.

Water samples were collected at consistent intervals and immediately filtered through 0.22 μm pore size nylon membrane filters for subsequent analysis. All the batch experiments were carried out in triplicate. The post-adsorption adsorbent samples were also collected, and dried at 80 °C for further analysis. The concentrations of residual phosphate were assessed using the ammonium molybdate spectrophotometric methods respectively, using UV-vis spectrophotometer (UV-1800, Shimadzu). The adsorption capacity (mg g^{-1}) was determined by eqn (1):

$$q_e = \frac{(C_i - C_e)V}{m} \quad (1)$$

Here, q_e denotes the amount of phosphate adsorbed at equilibrium (mg g^{-1}). C_i and C_e are the initial and equilibrium concentrations of phosphate (mg L^{-1}), respectively. m is the mass of adsorbent (g). V is the volume of adsorption solution (L).

The removal efficiencies were then calculated using the following equation:

$$R\ (\%) = \frac{C_i - C_e}{C_i} \times 100\% \quad (2)$$

where, R is the removal efficiency (%). C_i is the initial adsorbate concentration (mg L^{-1}), and C_e is the residual phosphorus concentration at equilibrium (mg L^{-1}).

2.5 Phosphate desorption experiments and adsorbent reusability

To evaluate the reusability of the tested adsorbents and recovery of adsorbed PO_4^{3-}, desorption experiments were performed on PO_4^{3-} loaded samples. The desorption of PO_4^{3-} was examined using two solvent systems; distilled water and NaOH solutions of varying concentrations, at different time intervals (5 to 75 min). The adsorbent materials were divided equally into two parts and dispersed in the respective solvent solutions. For each desorption experiment, 50 mL of either distilled water or NaOH solution was added to the PO_4^{3-} enriched material. The mixture was shaken at 150 rpm at 25 °C for 75 min and subsequently filtered as described in the adsorption experiments. The residual PO_4^{3-} concentrations in the supernatants were measured using a UV spectrophotometer.

Seven successive adsorption–desorption cycles were carried out to assess the reusability of the regenerated adsorbents, with

adsorption performance measured in each cycle. Prior to each re-adsorption experiment, the adsorbents were dried at 90 °C overnight and then reused for subsequent adsorption–desorption processes. The PO_4^{3-} desorption efficiencies (%) were calculated according to following equation:

$$\text{Desorption efficiency}(D_e) = \frac{C \times V}{q \times m} \times 100\% \quad (3)$$

Here, C (mg L^{-1}) represents the PO_4^{3-} concentration in the desorbed solution, q (mg g^{-1}) denotes the amount of PO_4^{3-} adsorbed before desorption, m (g) is the mass of adsorbent used in the desorption experiments, and V (L) refers to the volume of the desorbed solution.

2.6 Synthesis and evaluation of water-retention capacity of soil with PLC (phosphate loaded composite)

Phosphate-loaded composite (PLC) was prepared as follows: 0.25 g of Mg@NFC/BN was added to a flask containing 250 mL of 100 mg L^{-1} of $H_2PO_4^-$ aqueous solution. The mixture was maintained at 25 °C and agitated for 2 h, followed by filtration and drying at 80 °C until a constant weight was achieved.

To evaluate the soil water-retention capacity with PLC, sandy loam soils were collected from cultivated fields at IIT BHU, Varanasi (Eastern India). The samples were amended with varying ratios of PLC and soil and assessed for water-retention ratios. The experiment included four groups: (i) 100 g of air-

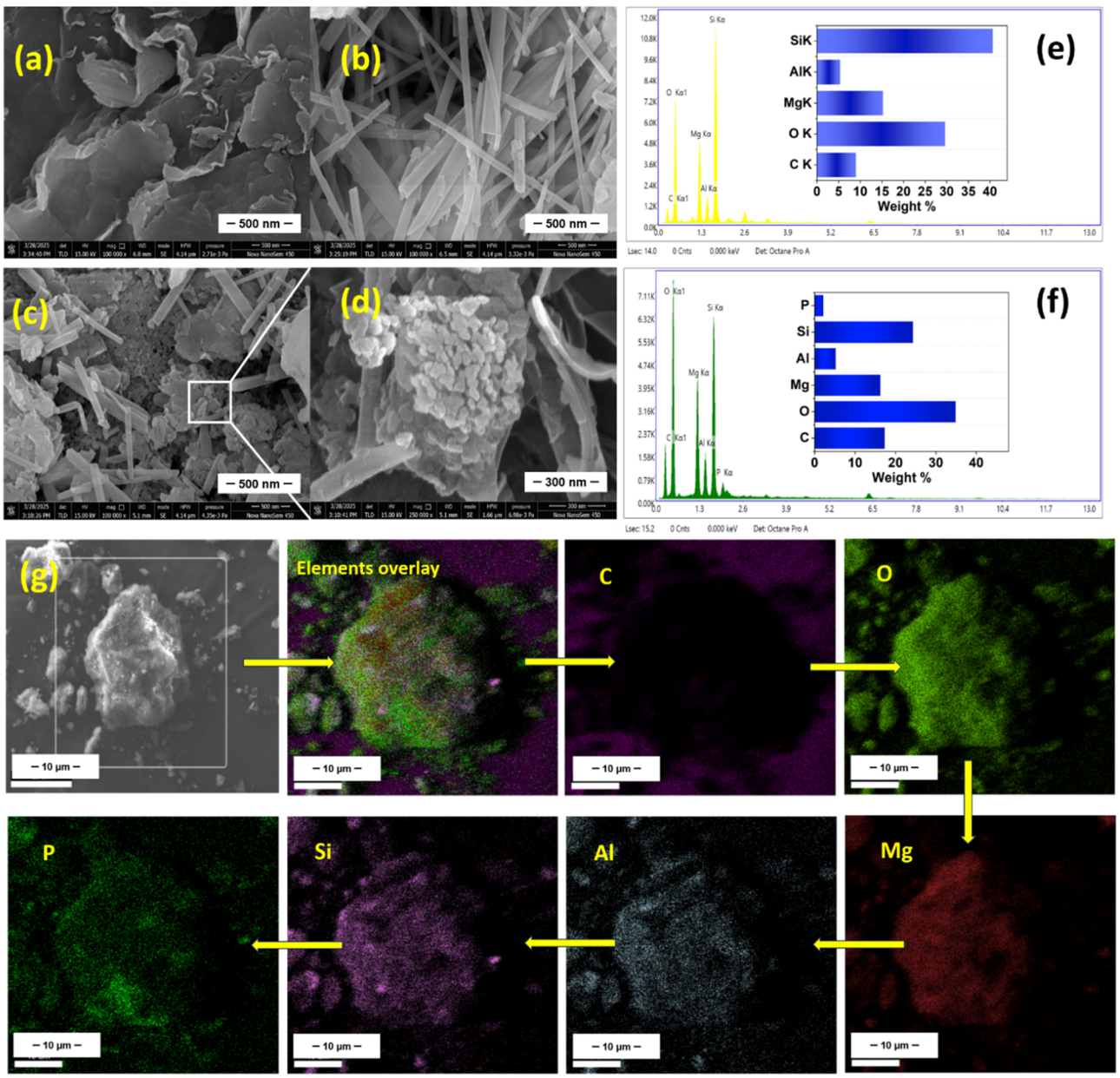

Fig. 2 SEM images of; (a) NFC/BN; (b & c) Mg@NFC/BN (pre and post phosphate adsorption respectively); (d) high resolution SEM micrograph of Mg@NFC/BN (post adsorption); (e & f) EDS spectra and corresponding element distribution content of Mg@NFC/BN (pre and post phosphate adsorption respectively) (g) EDS elemental mapping of C, O, Mg, Al, Si, and P of Mg@NFC/BN (after adsorption).

dried soil (control); (ii) 0.5 g of PLC mixed with 100 g of dry soil; (iii) 1 g of PLC mixed with 100 g of dry soil; and (iv) 2 g of PLC mixed with 100 g of dry soil. The samples were packed into PVC tubes with a diameter of 4.5 cm, where the bottom of each tube was sealed with four layers of 200-mesh nylon fabric.

The initial weight of the tubes was recorded as M_0. Tap water was gradually added from the top of each PVC tube until water percolated out from the bottom. Once the soil and PLC mixture were thoroughly saturated with water and no further percolation was observed, the tubes were weighed again and recorded as M_i. Subsequently, the tubes were maintained under identical environmental conditions and weighed at different time interval (M_F) alternately over a monitoring period of 30 days. The water-retention capacity (WRC%) for the soil samples was calculated using the following equation:

$$\mathrm{WRC}\% = \frac{M_F - M_0}{M_i - M_0} \times 100\% \quad (4)$$

3 Results and discussions

3.1 Physicochemical characterization of synthesized adsorbent

The surface morphology and elemental composition of the NFC/BN composite, as well as Mg@NFC/BN samples before and after phosphate sorption, were examined using Field Emission Scanning Electron Microscopy (FESEM) in tandem with Energy Dispersive X-ray Spectroscopy (EDS), with the results illustrated in Fig. 2. The FESEM micrograph of the NFC/BN composite reveals layered nanosheets characterized by a heterogeneous structure with wrinkled and folded edges, where NFC functions as a reinforcing agent within the bentonite clay matrix (Fig. 2a). It can be assumed that the absence of a distinct fibrous NFC structure in the images is due to its intercalation within the interlayer spaces of bentonite, likely facilitated by hydrogen-bonding interactions.[21] This structural integration enhances the composite's stability and dispersion characteristics, contributing to its improved performance in phosphate removal. The subsequent incorporation of magnesium into the NFC/BN composite induces exfoliation of the structure, leading to the formation of more randomly oriented rod-like fragments, thereby increasing the exposed surface area[22,23] (Fig. 2b). Following phosphate adsorption, the surface morphology of Mg@NFC/BN undergoes further modification, with the appearance of agglomerated nanostructures on the surface, suggesting adsorption of phosphate ions onto the composite (Fig. 2c). Fig. 2d shows the high-resolution surface architecture of the adsorbent after phosphate adsorption.

The EDS element content of adsorbent before and after adsorption are shown in Fig. 2e and f. The surface of Mg@NFC/BN mainly contained constituent elements such as C, O, Al and Si of NFC and bentonite well distributed on the synthesized composite surface. The detected presence of Mg (15.26%), confirms successful integration of Mg in NFC/BN composite which is in agreement with FTIR result. Furthermore, the post-adsorption samples exhibit the presence of P, indicating effective phosphate uptake. This validates the composite's enhanced adsorption efficiency, attributed to its structural characteristics and improved metal interaction sites.[24] The elemental composition, expressed in weight percentages, is further substantiated by EDX elemental mapping analysis images of phosphate loaded Mg@NFC/BN (Fig. 2g).

The formation of the hybrid composite was verified through Fourier Transform Infrared Spectroscopy (FT-IR) analysis, which involved comparing the surface modifications of functional group on NFC, BN, NFC/BN composite, and Mg@NFC/BN (pre and post adsorption) (Fig. 3a). For NFC, derived from natural cellulose, the FT-IR spectrum displayed distinct

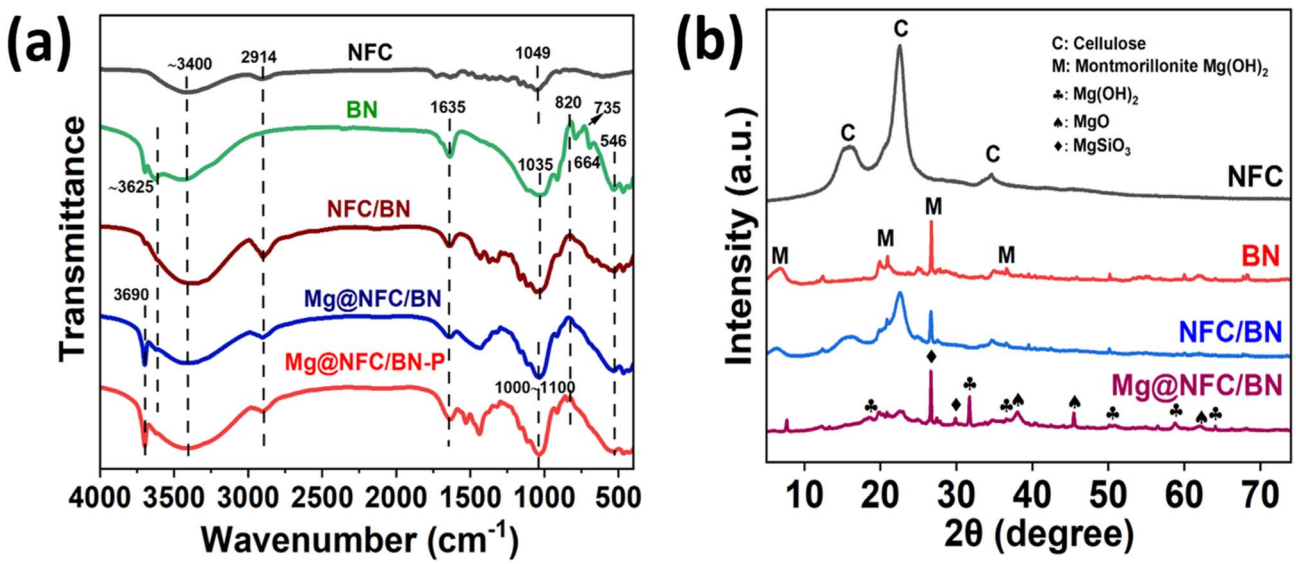

Fig. 3 FTIR spectra of (a) NFC, BN, NFC/BN composite, Mg doped NFC/BN (before and after adsorption); (b) XRD patterns of pristine NFC, BN NFC/BN composite and Mg doped NFC/BN.

absorption bands indicative of its functional groups. The broad band observed around 3400 cm^{-1} region corresponds to the stretching vibrations of O–H bonds including those associated with hydroxy functional groups, intermolecular hydrogen bonding, and free or bound water molecules. The distinctive peaks of cellulose are observed at approximately 2914 cm^{-1} and 1375 cm^{-1} (C–H bending), and 1140 cm^{-1} (C–O–C pyranose ring).[25] Additionally, the peaks at 1049 cm^{-1} and 893 cm^{-1} are associated with C–O stretching and glycosidic ether bond of β-1,4-glycosidic ring linkages between the D-glucose units in cellulose, respectively.[19] For raw bentonite, the figure shows characteristic bands at ~3410 cm^{-1} and ~1635 cm^{-1}, attributed to –OH stretching and H–O–H bending of interlayer water.[26] The sharp band observed at ~3625 cm^{-1} in bentonite corresponds to the stretching vibration of structural Al–OH groups within the montmorillonite lattice, confirming the presence of di-octahedral smectite. The strong band at 1035 cm^{-1} correspond to Si–O bond vibrations in montmorillonite, while Al–O vibrational peak appeared at 820 cm^{-1}.[27] The vibrational peak at 912 cm^{-1} corresponds to the –OH bending associated with $Al(OH)_3$ in the bentonite structure. The peaks at 735 cm^{-1}, and 464 cm^{-1} correspond to Si–O–Si vibrations, while the peaks at 664 cm^{-1} and 500 cm^{-1} are associated with the bending vibrations of octahedral Al–O–Si of bentonite.[28] The FT-IR spectrum of the synthesized NFC/BN composite exhibited a complex profile, demonstrating that all characteristic peaks of both NFC and BN were preserved; confirming hybridization between NFC and BN. Notably, the O–H stretching band ~3400 cm^{-1} becomes broader and is slightly shifted compared to its individual components, which is clearly observable in the graph. This broadening indicates enhanced hydrogen bonding between NFC hydroxyl groups and BN surface –OH sites. Minor shifts and intensity changes in the ~1030–1050 cm^{-1} region further suggest strong interfacial interactions and partial intercalation of NFC into bentonite layers. The FT-IR spectra of Mg-doped NFC/BN revealed a prominent peak at 3690 cm^{-1}, corresponding to the –OH stretching vibration in $Mg(OH)_2$, alongside a peak at 546 cm^{-1}, attributed to the Mg–O stretching vibration, confirming the successful incorporation of Mg into the composite.[29] The characteristic C–H stretching band of cellulose (~2914 cm^{-1}) displayed a reduction in intensity, likely due to structural modifications or interactions between Mg^{2+} and functional groups within the composite. Notably, reduction in intensity of the O–H stretching bands (~3400 cm^{-1} and 1635 cm^{-1}) clearly visible in the post-adsorption spectrum provides strong evidence for ligand exchange, where phosphate replaces surface –OH groups. Furthermore, the faint peaks observed at 833 cm^{-1} and 458 cm^{-1} were attributed to deformation vibrational modes of Al–O–Mg and Si–O–Mg bonds, indicating the presence of cation exchangeable Mg^{2+} onto the composite matrix, which is in agreement with EDS analysis.[30] Symmetric and asymmetric stretching vibrations within the 1000–1100 cm^{-1} range, attributed to phosphorus (P=O) functional group of phosphate ions, were clearly evident. Concurrently, the band at approximately 546 cm^{-1}, associated with Mg–O, nearly disappears, indicating direct involvement of Mg sites in phosphate binding. These findings provide clear evidence of adsorption of phosphate onto the synthesized adsorbent.

X-ray Diffraction (XRD) profiles of pristine NFC, BN, NFC/BN, and Mg@NFC/BN composites were analysed to determine the phase composition, sample purity, and structural transitions (Fig. 3b). The diffraction pattern of raw bentonite confirmed its enrichment in montmorillonite as the predominant clay phase, with characteristic peaks observed at 6.99°, 19.86°, 20.9°, 24.9°, 26.68°, 34.88°, and 36.6° (reference no. 01-088-0891 and 00-033-1200).[31] For NFC, peaks at 16.1°, 22.4°, and 34.5° correspond to the (110), (200), and (004) crystallographic planes of cellulose I, confirming its structural integrity.[32] The XRD pattern of the NFC/BN composite exhibited integration of primary diffraction peaks from both NFC and BN, accompanied by a decrease in peak intensity. This reduction in intensity suggests successful composite formation, where NFC is well distributed across the bentonite surface and intercalated within the clay layers. Upon Mg ion incorporation into the NFC/BN matrix, the XRD pattern of Mg@NFC/BN revealed further attenuation of peak intensities, along with the appearance of new peaks, indicative of magnesium-containing phases such as MgO, $Mg(OH)_2$, and $Mg(SiO_3)$ (reference no: 00-002-1207, 01-082-2454 and 01-082-1644).[33] These structural modifications confirm the successful integration of Mg ions into the composite matrix. Furthermore, the XRD findings are in strong agreement with FT-IR and XPS analyses, further supporting the structural and compositional changes in Mg@NFC/BN composite.

3.2 Phosphate removal/uptake studies

3.2.1 Preliminary assessment. The removal efficiency of native nanofibrillated cellulose, raw BN, NFC/BN composite, and Mg@NFC/BN at varying ratios were investigated, and their adsorption capacities towards phosphate were evaluated. Fig. 4a shows that the overall adsorption performance of NFC/BN composite and Mg doped NFC/BN composite on phosphate is better than that of pristine NFC and raw BN. The adsorption capacities of NFC, BN, NFC/BN composites, and Mg@NFC/BN showed a trend of $Mg@NFC_1/BN_1 > NFC_1/BN_1 > NFC_2/BN_1 > NFC_1/BN_2 > NFC_4/BN_1 > NFC_1/BN_4 > NFC > BN$. This behaviour is ascribed to the synergetic effect between nanofibrillated cellulose and bentonite clay, which promotes cooperative interactions, resulting in a higher adsorption capacity than that of either material alone. Among the NFC/BN composites, NFC_1/BN_1 depicted the highest phosphate removal efficiency of 80.1%. This is because NFC provides abundant hydroxy groups, facilitating hydrogen bonding and electrostatic interactions with phosphate while bentonite, a layered clay, enhances adsorption by providing additional binding sites and interlayer spaces for phosphate capture. In addition, the balanced proportion of NFC and BN optimized the surface properties and adsorption sites of the composite adsorbent, thereby improving its overall performance. Conversely, NFC_4/BN_1 and NFC_1/BN_4 exhibited lower adsorption efficiency, even in composite form. This may be attributed to the increased viscosity at higher NFC concentrations, which impedes the uniform dispersion of NFC and BN. Notably, a 4 : 1

NFC-to-BN ratio was not utilized for metal doping due to anticipated challenges in maintaining an even and effective distribution.[34] Similar limitation lies in nanocellulose–clay composites at higher clay loadings *i.e.*, maintaining dispersion, as increased clay content does not necessarily corelate with improved adsorption capacity. For instance, when bentonite clay concentration was increased from 1 to 4, the phosphate adsorption capacity of NFC/BN composite decreased from 16.2 mg g^{-1} to 9.15 mg g^{-1}. This decline is likely due to clay aggregation and reduced pore accessibility at higher clay concentrations.[35] Given its excellent adsorption performance and cost-effectiveness, NFC_1/BN_1 ratio was taken into consideration for Mg. The resulting Mg-doped NFC_1/BN_1 composite exhibited the highest adsorption capacity of approximately 19.2 mg g^{-1} and removal efficiency of 88.6%. This enhancement may be resulting from metal ion modification, which increases phosphate adsorption capacity by reducing the negative charge and elevating the isoelectric point (PZC) of the NFC/BN composite.[36] Taking into account the adsorption performance, magnesium doped NFC/BN composite with optimal ratio combination was chosen for subsequent studies.

3.2.2 Effect of pH. The pH significantly influences the surface charge of the adsorbent as well as the removal and uptake of ions at the water–adsorbent interface (Fig. 4b). The speciation of orthophosphate, including H_3PO_4, $H_2PO_4^-$, HPO_4^{2-}, and PO_4^{3-}, is governed by the solution pH values of <2.0, 2.0–7.0, 7.0–12.0 and >12.0 respectively, based on their corresponding dissociation constants (pK_a).[37] The adsorption free energy of $H_2PO_4^-$ was lower than that of HPO_4^{2-}, indicating that $H_2PO_4^-$ was more readily adsorbed onto the surfaces of Mg@NFC/BN composites compared to HPO_4^{2-}.[38] The effect of pH on the removal of phosphate was assayed at different pH values ranging from 2 to 11. Mg@NFC/BN demonstrated outstanding phosphate removal efficiency under acidic conditions, while an increase in solution pH led to a noticeable reduction in the adsorption performance. As shown in the figure, a consistent and effective removal was observed within the pH range of 4 to 7, where $H_2PO_4^-$ was the dominant species, facilitating strong binding with Mg^{2+} and resulting in high adsorption efficiency. However, at pH levels above 7, a gradual decline in adsorption capacity was evident. The figure indicates that the highest removal percentage and adsorption capacity within pH 4 to 9 varied between 93.8 to 78.57% and 20.01 to 14.89 mg g^{-1}, respectively. This trend can be attributed to the influence of the adsorbent's surface charge.[39] As observed in Fig. 4c, the point of zero charge (PZC) of Mg@NFC/BN was

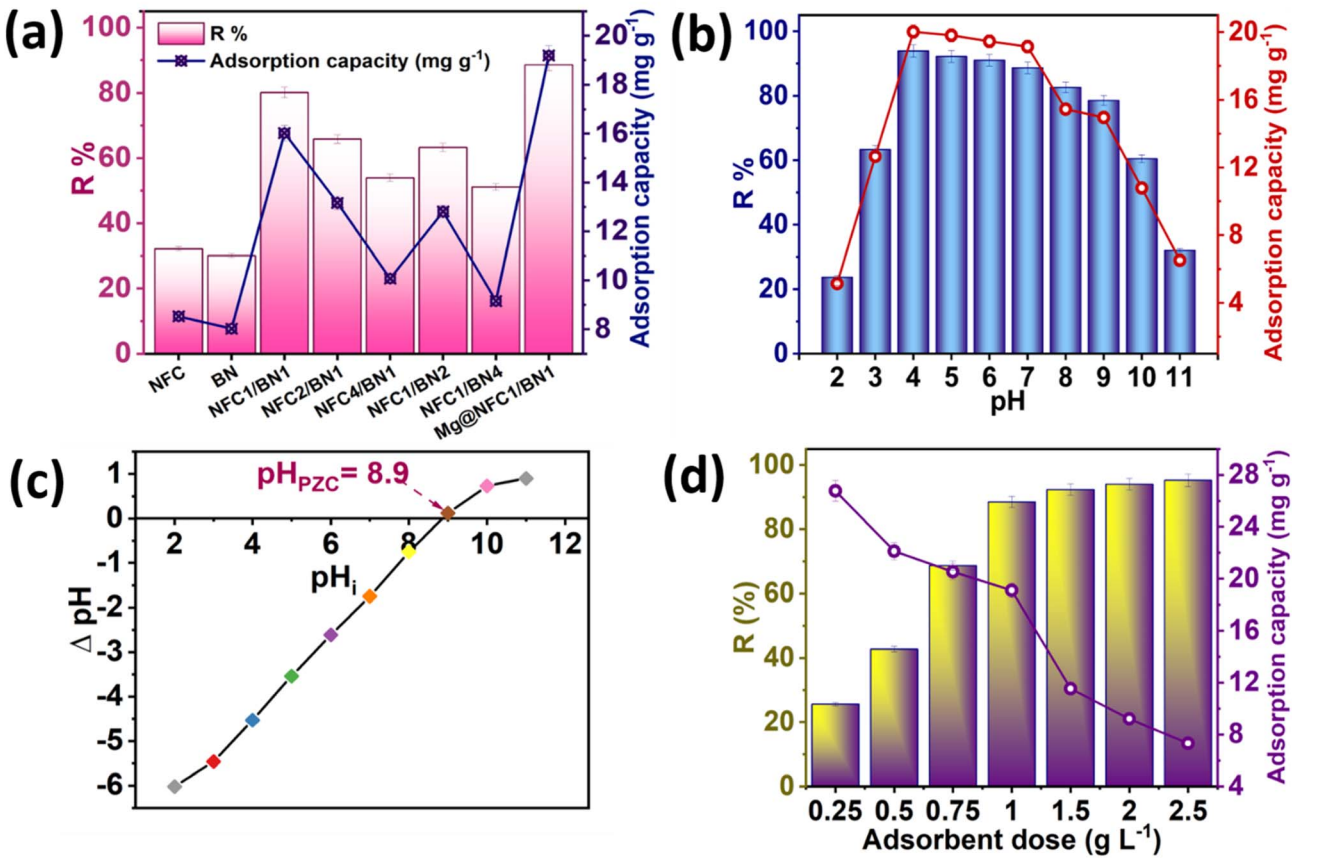

Fig. 4 (a) Pre-screen adsorption of pristine NFC, BN, NFC/BN composites (with varying molar ratios) and Mg doped NFC/BN; (b) effect of different pH values (2–11) on phosphate removal (initial conc. 20 mg L^{-1}, dose 1 g L^{-1}, contact time 90 min); (c) pH_{PZC} value of Mg@NFC/BN and; (d) effect of adsorbent dose (0.25–2.5 g L^{-1}) on phosphate removal by Mg@NFC/BN (initial conc. 20 mg L^{-1}, initial pH 7.0 ± 0.2, contact time 90 min).

identified at approximately 8.9. This suggests that when the pH is below 8.9, the surface of the adsorbent becomes protonated, procuring a positive charge that enhances electrostatic attraction with anionic phosphate species in the solution. In contrast, when the pH exceeds 8.9, the surface charge shifts to negative, leading to electrostatic repulsion of anions and a subsequent decline in phosphate adsorption capacity. Post sorption, the PZC of the adsorbent shifted to 7.6, indicating a pronounced reduction from its initial value. This decrease was attributed to surface charge neutralization resulting from site protonation occurring near the metal-loaded surface within the shear plane.[40] At pH $\geq$ 3, the adsorbent exhibited relatively lower removal efficiency and adsorption capacity, approximately 23.7% and 5.14 mg g^{-1}, respectively. This reduction is associated to phosphate speciation, where H_3PO_4 predominates, making adsorption less favourable. Alternatively, when the pH surpasses 9.0, a sharp decline in adsorption capacity is observed.[41] This is likely due to the high concentration of hydroxide ions competing with phosphate for active adsorption sites, coupled with increased electrostatic repulsion in the highly alkaline medium. Furthermore, the decrease in phosphate removal at elevated pH levels is also associated with a shift in phosphate speciation from $H_2PO_4^-$ and HPO_4^{2-}, in concurrence with a reduction in protonation rates.

Additionally, when the initial pH ranged between 3 and 6, the equilibrium pH of the solution elevated to around 9.0. This increase in pH was mainly due to a ligand exchange reaction, in which $H_2PO_4^-$ replaced –OH groups on the composite surface, leading to inner sphere complexation and the release of OH^- into the solution.[42] The findings indicated that Mg@NFC/BN is a sustainable option for phosphate removal in conventional wastewater treatment, as the pH of wastewater typically ranges from 5.0 to 8.0.

3.2.3 Effect of adsorbent dose. The effect of adsorbent dosage on phosphate removal was investigated to determine the optimal dosage for maximum removal efficiency while maintaining constant volume and initial phosphate concentration (Fig. 4d). The results indicate that optimizing this parameter can significantly reduce the required adsorbent amount while achieving high removal efficiency. As the dosage of Mg@NFC/BN increased from 0.5 to 2.5 g L^{-1}, the phosphate removal efficiency improved markedly from 42.7% to 91.4%. However,

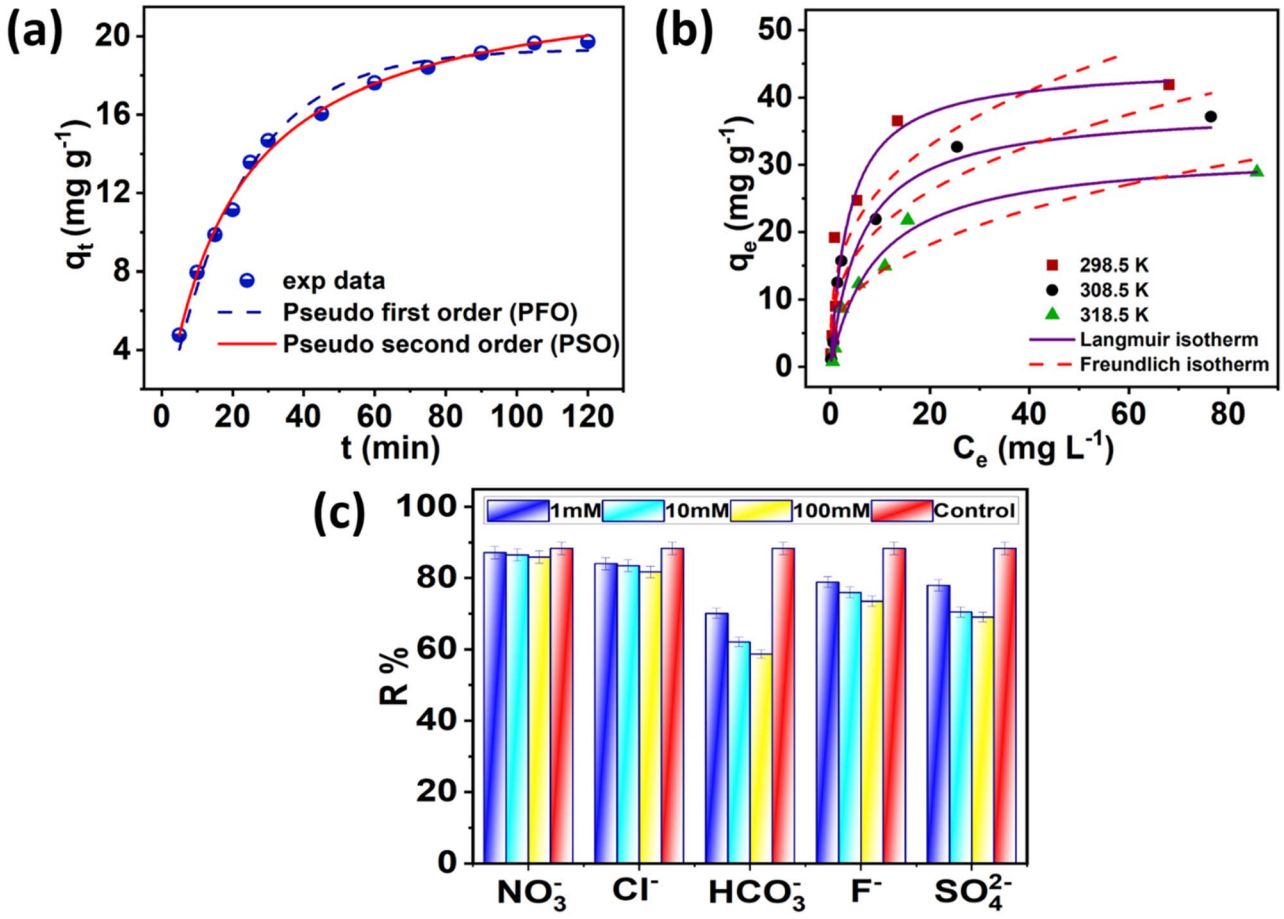

Fig. 5 (a) Effect of different contact time (0–120 min) on phosphate removal by Mg@NFC/BN and adsorption kinetics (initial conc. 20 mg L^{-1}, dose 1 g L^{-1}, initial pH 7.0 $\pm$ 0.2); (b) effect of different initial concentration (2, 5, 10, 20, 30, 50 and 100 mg L^{-1}) on phosphate removal by Mg@NFC/BN and adsorption isotherm (at varying temperature (298.5 K, 308.5 K and 318.5 K), adsorbent dose 1 g L^{-1}, initial pH 7.0 $\pm$ 0.2, contact time 90 min); the points and lines depict the experimental data and fitting curves of kinetic and isotherm models, respectively; (c) effect of co-existing anions typically found at different values in wastewaters (1, 10, 100 mM concentration).

Table 1 Kinetic parameters of the phosphate removal/uptake onto Mg@NFC/BN

Models	Parameters	Mg@NFC/BN
Pseudo-first-order kinetic model	$q_{e,cal}$ (mg g^{-1})	23.27
	k_1 (min^{-1})	0.046
	R^2	0.96
Pseudo-second-order kinetic model	$q_{e,cal}$ (mg g^{-1})	19.33
	k_2 (g mg^{-1} min^{-1})	0.002
	R^2	**0.99**

the phosphate adsorption capacity exhibited a decreasing trend with increasing adsorbent dosage. This decline could be attributed to the agglomeration of excess adsorbent, that limits the effective utilization of adsorption sites, thereby reducing the adsorption capacity.[43] Notably, an adsorbent dosage of 1 g L^{-1} exhibited a removal efficiency of 88.5%, which corresponded well with a favourable adsorption capacity of 19.17 mg g^{-1}. Therefore, taking into account both economic feasibility and removal performance, 1 g L^{-1} was deemed as the optimal dosage.

3.3 Adsorption kinetic studies

The experimental data were modelled by pseudo-first-order (PFO) and pseudo-second-order (PSO) models (Fig. 5a). The nonlinear expressions of these models are listed in SI file. As evident from the figure, the phosphate adsorption onto Mg@NFC/BN proceeded rapidly during the initial 30 min, followed by a slower phase until equilibrium was reached at approximately 90 min. This trend can be attributed to the progressive saturation of available adsorption sites. According to the kinetic parameters summarized in Table 1, both the pseudo-first-order and pseudo-second-order models yielded high correlation coefficients ($R^2 > 0.9$), indicating good agreement with the experimental data. However, a closer comparison of the R^2 values reveals that the pseudo-second-order model provided a better fit, with a higher R^2 value when considering the second decimal place. Furthermore, the calculated adsorption capacity ($q_{e,cal}$) derived from the pseudo-second-order model closely matched the experimental data (q_{exp}), confirming that the adsorption of phosphate onto Mg@NFC/BN is predominantly governed by chemisorption mechanism.[44]

3.4 Adsorption isotherm studies

To gain deeper insight into the solid–liquid adsorption behaviour, both Langmuir and Freundlich isotherm models were applied to describe the equilibrium data. The equations of nonlinear isotherm models are given in SI file. The adsorption isotherm data for phosphate on Mg@NFC/BN at varying initial concentrations and different temperatures (298.5 K, 308.5 K, and 318.5 K) is presented in Fig. 5b. As shown, the adsorption capacity (q_{max}) increased with increasing initial phosphate concentrations, which can be attributed to the enhanced mass transfer driving force at higher concentrations.[45] At an initial phosphate concentration of 20 mg L^{-1} and temperature of 298.5 K, the adsorption capacity reached 19.2 mg g^{-1}. Moreover, the gradual decline in the maximum adsorption capacity (q_{max}), as estimated from the Langmuir isotherm model with increasing temperature, suggesting that the adsorption process is likely exothermic in nature. The corresponding isotherm constants and regression coefficients with respect to different temperatures are summarized in Table 2. Notably, the Langmuir model exhibited higher correlation coefficients ($R^2 \geq 0.99$) compared to the Freundlich model ($R^2 \geq 0.88$) at 298.5 K, indicating a better fit to the experimental data. These results imply that phosphate adsorption onto Mg@NFC/BN occurs predominantly *via* monolayer adsorption on a homogeneous surface.[46]

3.5 Effect of co-existing anions

Wastewater from industrial processes, mining and metal processing typically contains other co-existing anions such as Cl^-, SO_4^{2-}, and CO_3^{2-} (HCO_3^-) along with PO_4^{3-}. During the

Table 2 Isotherm parameters of the phosphate removal/uptake onto Mg@NFC/BN at different temperatures (298.5 K, 308.5 K and 318.5 K)

Models	T (K)	Parameters	Mg@NFC/BN
Langmuir isotherm model	298.5	q_{max} (mg g^{-1})	44.7
		K_L (L mg^{-1})	0.26
		R^2	**0.99**
	308.5	q_{max} (mg g^{-1})	38.45
		K_L (L mg^{-1})	0.16
		R^2	0.96
	318.5	q_{max} (mg g^{-1})	32.05
		K_L (L mg^{-1})	0.1
		R^2	0.97
Freundlich isotherm model	298.5	K_F (mg g^{-1}) (L mg^{-1})$^{1/n}$	12.67
		n_F	3.14
		R^2	0.88
	308.5	K_F (mg g^{-1}) (L mg^{-1})$^{1/n}$	9.67
		n_F	3.02
		R^2	0.92
	318.5	K_F (mg g^{-1}) (L mg^{-1})$^{1/n}$	6.05
		n_F	2.73
		R^2	0.89

production processes in certain industrial parks, the wastewater generated contains lithium hexafluorophosphate ($LiPF_6$) that contains a significant amount of fluoride (F^-) and phosphate ions.[47] Additionally, nitrogen and phosphorus are common pollutants in wastewater originated from domestic sewage, agricultural runoff, industrial effluents, aquaculture waste, and landfill leachate. These anions can impact the phosphate removal efficiency of adsorbents. Hence, to evaluate the adsorption behaviour of Mg@NFC/BN for phosphate in complex solutions *i.e.*, the presence of various interfering anions, we performed competitive adsorption experiments using different anion concentrations (1 mM L^{-1}, 10 mM L^{-1}, and 100 mM L^{-1}). Fig. 5c illustrates the phosphate removal efficiency of the synthesized adsorbent, and it can be seen that at lower concentrations of all coexisting ions, the removal efficiency remains largely unaffected. In contrast, as the concentration of these ions increases, their impact on the removal efficiency is only slightly affected. The results reveal that phosphate removal efficiency of Mg@NFC/BN is minimally affected in the presence of Cl^- (2.33%), NO_3^- (1.27%), and F^- (5.41%) ions, despite an increase in their concentration from 1 to 100 mM L^{-1}. The inhibitory effect of these anions on phosphate adsorption follows the order; $F^- > Cl^- > NO_3^-$. This can be attributed to the fact that competition from other anions is influenced by their charge density and ionic radii. The ionic radii of $H_2PO_4^-$ (~0.24 nm) is relatively larger and has higher charge density than Cl^- (0.18 nm), NO_3^- (0.179 nm), and F^- (0.13 nm). This suggests that among these anions, fluoride exhibits the strongest competition due to its small size and high charge density, chloride shows moderate competition but is less effective than F^- while NO_3^-, due to its large size and delocalized charge, has the weakest competition and least inhibitory effect.[48] The inhibition effect of SO_4^{2-} (100 mM L^{-1}) led to a notable decrease in the phosphate removal efficiency of Mg@NFC/BN. This can be ascribed to the ionic radii of SO_4^{2-} ions (0.23 nm) which is comparable to the ionic radii of phosphate.[49] Despite lower charge density, it strongly interacts with positively charged adsorption sites, leading to competitive adsorption. However, phosphate forms inner-sphere complexes through strong covalent bonding while sulphate typically forms outer–sphere complexes through weak electrostatic interactions, but at high concentrations, it can still disrupt phosphate adsorption by blocking active sites. However, the phosphate removal efficiency could only decrease by 19.2% at concentration of 100 mM L^{-1}. Among various anions, HCO_3^- exhibited the most significant impact, reducing phosphate removal

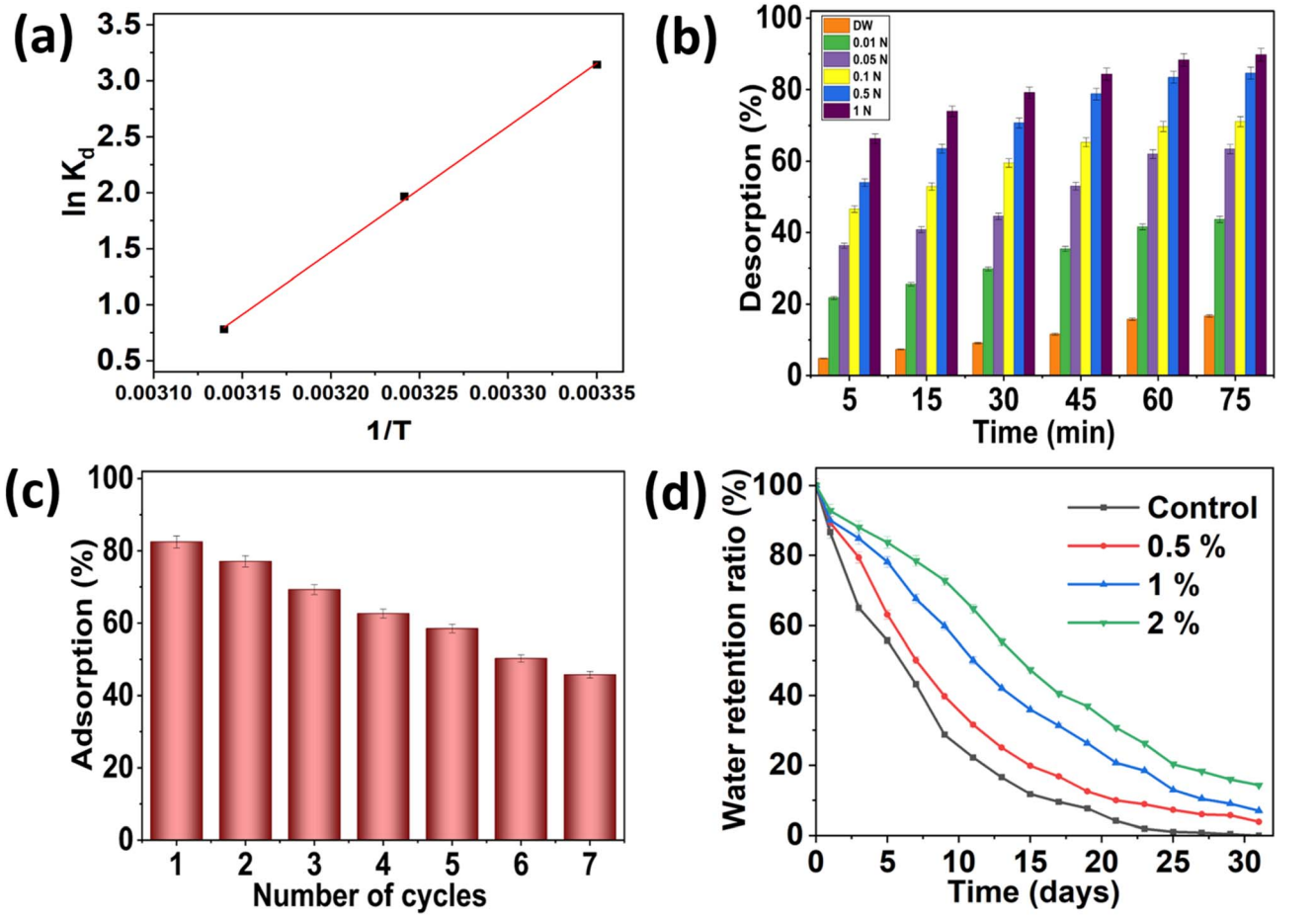

Fig. 6 (a) Linear plot of ln K_d *versus* 1/*T*; (b) phosphate desorption using distilled water and varying concentration of alkaline solution at different time intervals; (c) number of cycles regarding adsorbent reusability for phosphate recovery; (d) water-retention property of soil samples: (■) control (without PLC), (●) 0.5% PLC, (▲) 1% PLC and (▼) 2% PLC.

efficiency by 18.24%, 26.3% and 29.68% at concentrations of 1, 10, and 100 mM L^{-1}, respectively, compared to the control group. As the concentration of HCO_3^- increased, phosphate removal efficiency further declined. The presence of HCO_3^- could elevate the solution's pH, which was not favourable to phosphate adsorption. However, high concentrations of HCO_3^- were seldom encountered in actual wastewater, enabling Mg@NFC/BN to effectively adsorb phosphate through inner-sphere complexation.[44]

3.6 Adsorption thermodynamic studies

The spontaneity and thermodynamic behaviour of phosphate adsorption onto Mg@NFC/BN were evaluated based on thermodynamic parameters, including changes in Gibbs free energy (ΔG^0), enthalpy (ΔH^0), and entropy (ΔS^0), calculated using the equations provided in the SI file. The linear plot of $\ln(q_e/C_e)$ *versus* $1/T$ (Fig. 6a) and the corresponding thermodynamic data are provided in SI file. The negative values of ΔG^0 at all studied temperatures confirm that phosphate adsorption is both feasible and spontaneous under experimental conditions.[50] Furthermore, increasing ΔG^0 values shifting from -7.84 kJ mol^{-1} at 298.5 K to -2.109 kJ mol^{-1} at 318.5 K, indicating that the adsorption process is more favourable at lower temperatures, with a gradual decline in spontaneity as temperature rises.[51] The ΔH^0 value of -93.37 kJ mol^{-1} suggests an exothermic adsorption process, that is consistent with isothermal studies, demonstrated a decrease in adsorption capacity with increasing temperature. Additionally, the negative ΔS^0 indicates a decrease in interface randomness between Mg@NFC/BN and aqueous solution during adsorption process, possibly due to strong interactions such as chemisorption, which is in line with observations from kinetic studies.

3.7 Desorption performance

To promote adsorbent reusability and enable the recycling of PO_4^{3-} as a fertilizer resource, it is essential to investigate its desorption behaviour following adsorption saturation. In this study, PO_4^{3-} desorption was assessed by comparing the total amount desorbed to the total initially adsorbed, using both water and alkaline solutions of varying concentrations. The choice of alkaline solvents was motivated by the observed decline in adsorption efficiency with increasing pH, suggesting that higher alkalinity facilitates the release of PO_4^{3-} from adsorbent surfaces. As illustrated in Fig. 6b, desorption efficiency was strongly influenced by both contact time and solvent concentration. PO_4^{3-} release increased steadily with time, reaching its maximum within 75 minutes. Similarly, increasing solvent concentration from 0.01 to 1 N enhanced desorption, yielding optimum rate of around 90%.

This effect can be attributed to competitive adsorption between OH^- and PO_4^{3-} ions at mineral binding sites. The desorption experiments were conducted under ambient temperature conditions, further demonstrating the suitability of the tested minerals for practical adsorbent regeneration. However, regenerated adsorbent exhibited relatively lower adsorption capacities (mg g^{-1}) and removal efficiencies (%) than freshly prepared adsorbents, primarily due to surface erosion, progressive loss of active sites, and structural transformation of the adsorbent matrix. Nevertheless, the adsorbent exhibited an initial adsorption capacity of 17.05 mg g^{-1} in the first regeneration cycle, with only 24.9% reduction observed after the seventh cycle, thereby demonstrating its high stability and regeneration potential (Fig. 6 c).

3.8 Water retention capacity of soil with PLC

Water retention refers to the ability to store and retain water in soil, which helps mitigate the effects of extreme climatic events and reduces the risk of flooding.[52] To evaluate this, the water-retention capacity of soil was examined under varying PLC application rates (Fig. 6d). Results demonstrated that incorporating PLC significantly improved the soil's ability to retain water. After 30 days of incubation, soils treated with 0.5%, 1%, and 2% PLC exhibited 3.86%, 7.03%, and 14.34% higher water retention, respectively, compared to the control group (without PLC). In the control group, water retention rapidly dropped to around 50% by the 6th day. However, in soils amended with PLC, this threshold was reached on 7th, 11th, and 14th day, depending on the PLC application rate of 0.5%, 1% and 2% respectively. By the 25th day, the control soil had nearly lost all retained moisture, whereas the soil samples with 0.5%, 1%, and 2% PLC still maintained 7.31%, 12.99%, and 20.34% water content, respectively. This enhancement is largely attributed to the hydrophilic properties cellulosic materials, along with the increased porosity resulting from the integration of bentonite into the cellulosic structure.[53] Soil amended with PLCs exhibited higher water retention than reported by Wen *et al.*[54] In comparison, soil containing 2% BSRF, developed by this group, retained only 10.6% water after 30 days, highlighting the superior water-holding capacity of PLCs. Similarly, Wang *et al.* observed in their study that soil with 2% MSCF retained only 13.3% water on the 27th day, which is lower than the water retention reported for PLCs in the present study.[55] Overall, these results indicate that using PLC can substantially boost the soil's ability to retain water, thereby contributing to effective water conservation, especially in arid and semi-arid regions.

3.9 XPS studies and proposed adsorption mechanism

X-ray Photoelectron Spectroscopy (XPS) patterns of Mg@NFC/BN samples before and after adsorption were compared to analyze the chemical states of elements involved in phosphate uptake/removal and gain detailed insights into the interaction mechanism at the solid/water interface (Fig. 7). As anticipated, the result of survey scan exhibited all the characteristic peaks of elements involved and successful Mg engineering on NFC/BN surface (Fig. 7a). Furthermore, the emergence of P 2p peak in the XPS spectra after adsorption clearly validates the uptake of phosphate onto the surface. As illustrated in high resolution XPS spectra of P 2p (Fig. 7b), it showed a characteristic doublet, which can be deconvoluted into two distinct peaks, corresponding to P–O ($2P_{1/2}$) and P═O ($2P_{3/2}$) positioned at 132.8 eV and 133.7 eV.[56] The observed doublet separation $P_{3/2}$–$P_{1/2}$ equals 0.89 eV, which indicate presence of phosphate groups (PO_4^{3-}

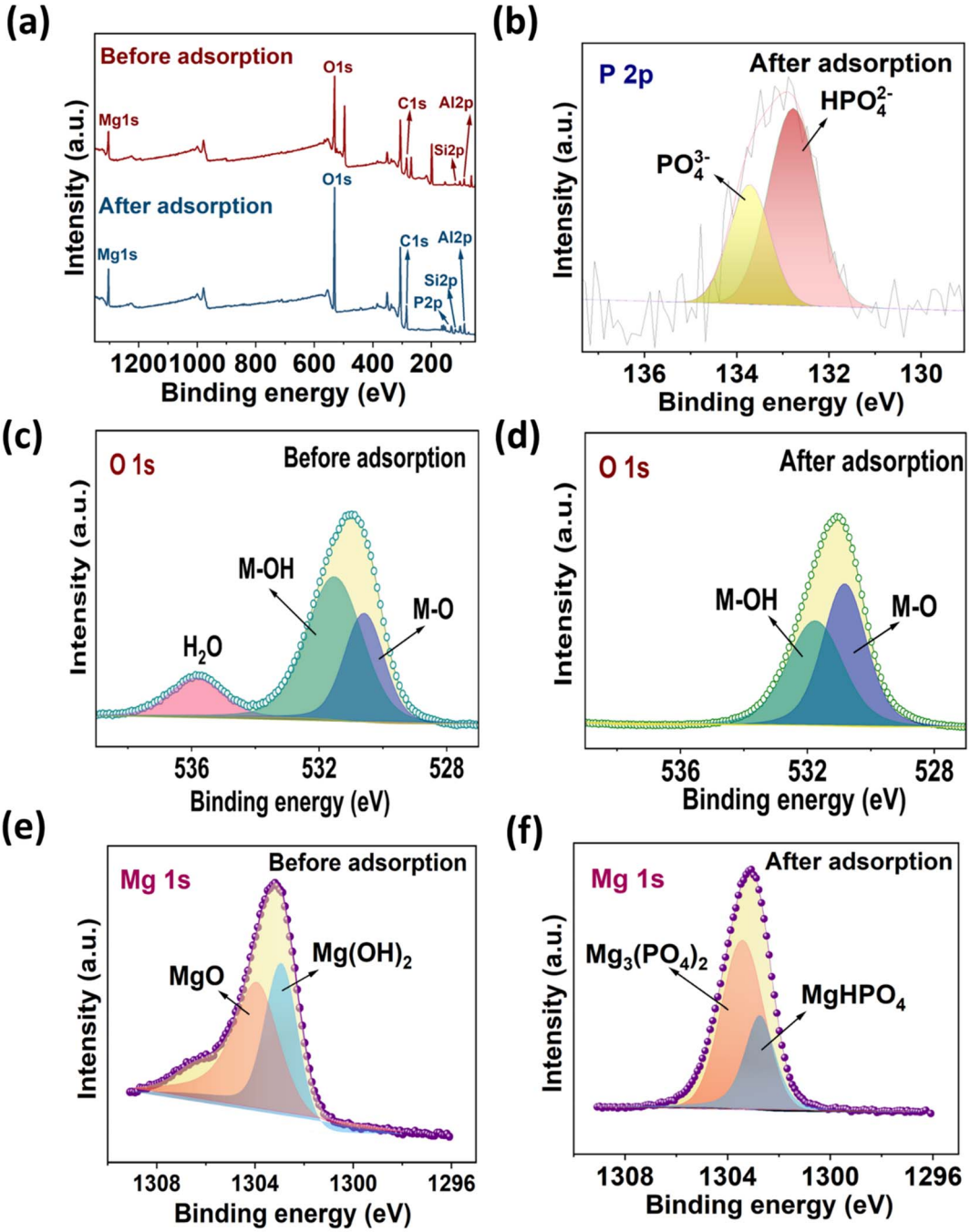

Fig. 7 (a) XPS spectra of Mg@NFC/BN prior to and post phosphate adsorption: (b) P 2p spectra (post adsorption); (c & d) O 1s spectra (pre and post adsorption); and (e & f) Mg 1s spectra (pre and post adsorption).

and HPO_4^{2-}) respectively, indicating successful adsorption of phosphate ions over the adsorbent's surface.[57]

As shown in Fig. 7c, the high-resolution O 1s spectrum of Mg@NFC/BN before adsorption was deconvoluted into three distinct peaks at 530.6 eV, 531.5 eV, and 535.83 eV. These peaks correspond to lattice oxygen (O_L), hydroxy oxygen (O_H), and physisorbed water, respectively, based on the binding energies of different oxygen species.[40,58] The O_L and O_H components represent metal–oxygen (M–O) and metal–hydroxy (M–OH) bonds, respectively. Prior to adsorption, the surface was dominated by M–OH species, reflecting the abundance of hydroxyl groups associated with Mg, Al, and Si sites. After phosphate adsorption (Fig. 7d), the relative peak area of M–OH species decreased markedly by 10.1%, accompanied by a corresponding increase in the M–O component by 22.3%, while the physisorbed water peak nearly disappeared (Table 3). This redistribution of oxygen species provides strong evidence for ligand exchange between surface –OH groups and phosphate ions, leading to the formation of stable M–O–P inner-sphere complexes.

Table 3 Relative peak area (%) of O 1s and Mg 1s components of Mg@NFC/BN before and after phosphate adsorption

Spectrum	Component	Binding energy (eV)	Before adsorption (%)	After adsorption (%)
O 1s	M–O	~530.6	30.1	52.4↑
O 1s	M–OH	~531.5	57.7	47.6↓
O 1s	H_2O	~535.8	12.2	~
Mg 1s	Mg–O	~1304	55.3	71.1↑
Mg 1s	Mg–OH	~1303.01	44.7	28.9↓

Table 4 Comparative study of functionalized bentonite, cellulose, and their composites for contaminant removal reported in the literature

Material type	Modification/ functionalization	Max adsorption capacity (mg g^{-1})	Key mechanism	Limitations	References
Functionalized bentonite	Mg–bentonite, La–bentonite, Zr–bentonite	12–30	—	Particle aggregation, moderate selectivity, regeneration issues	60–62
Functionalized cellulose	Carboxymethylation, amination, metal impregnation	5–15	Electrostatic interaction, H-bonding	Low affinity for anions, slow kinetics, poor aqueous stability	63–65
Cellulose–clay composites (without metal doping)	Cellulose–kaolinite/ bentonite	10–18	Synergistic adsorption *via* hydroxy groups & clay layers	Still negatively charged, limited selectivity for phosphate	23, 66 and 67
Other metal-doped biocomposites	Mg-biochar, Ca-cellulose composites	15–25	Inner-sphere complexation with phosphate	Costlier synthesis routes, reduced stability over cycles	7, 68 and 69
Mg@NFC/BN	Mg-doped nanofibrillated cellulose–bentonite composite	19.2 mg g^{-1} (88.6% removal)	Synergistic effect of NFC + BN + Mg (protonation, electrostatic interaction, ligand exchange → inner-sphere complexes)	—	Present study

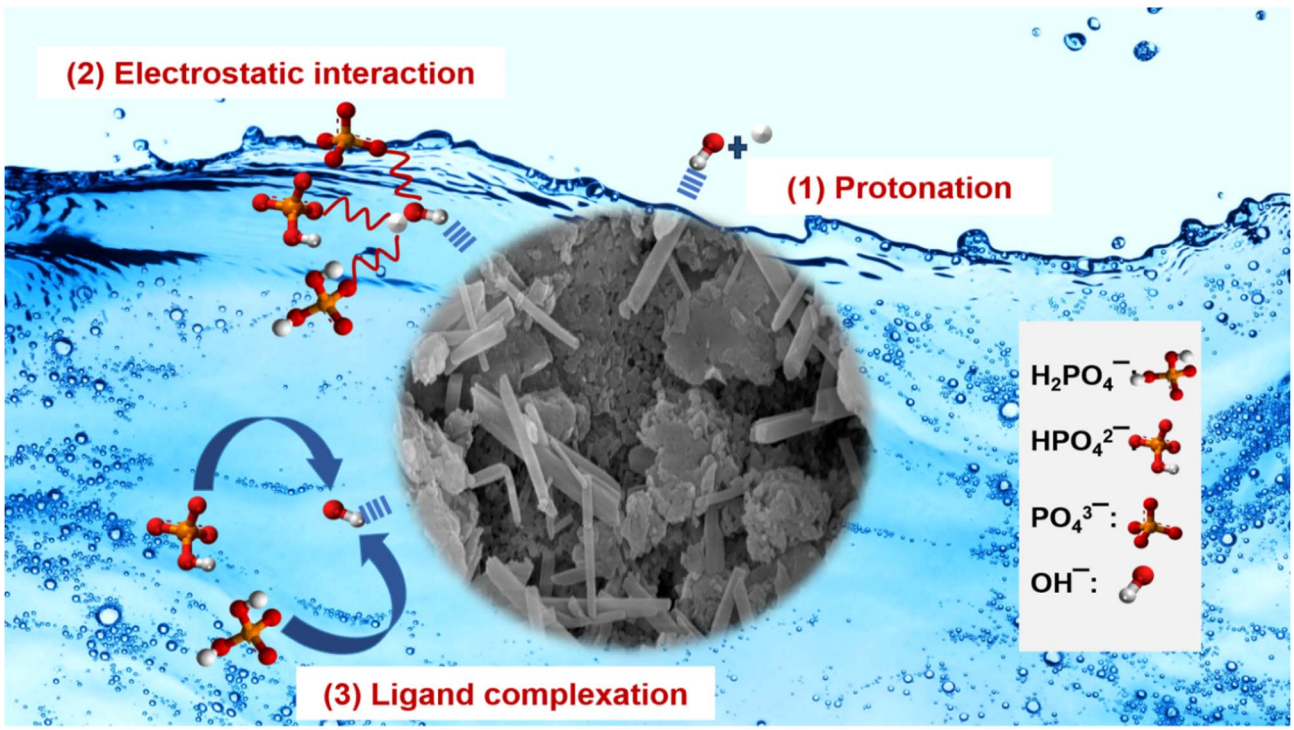

Fig. 8 Representation of adsorption mechanisms for phosphate removal on Mg doped NFC/BN.

In the Mg 1s spectra (Fig. 7e and f), the deconvoluted peaks at 1304 eV and 1303.01 eV corresponding to Mg–O and Mg–OH shifted to lower binding energies (1303.42 eV and 1302.7 eV) post adsorption respectively,[59] accompanied by a quantitative decrease in the Mg–OH peak area and an increase in Mg–O-related species as indicated in Table 4. These changes indicate direct coordination of phosphate with Mg centres, resulting in the formation of Mg–phosphate complexes such as $Mg_3(PO_4)_2$ and $MgHPO_4$. Also, the quantitative XPS findings are in agreement with FTIR results, where the attenuation of Mg–O vibrations (~546 cm^{-1}) and surface –OH stretching bands, together with the emergence of phosphate-related bands (1000–1100 cm^{-1}), further corroborate ligand exchange and inner-sphere complexation.

Combining all previous experimental findings, it can be seen that Mg@NFC/BN can effectively adsorb phosphate. Table 4 represents comparative analysis of the present study with previous studies conducted using cellulose, clay or their composites for the removal of various contaminants. Fig. 8 illustrated the possible mechanisms for phosphate removal/uptake by Mg@NFC/BN. In summary, the optimization studies, together with advanced analytical characterization, provide a comprehensive understanding of the adsorption mechanism of Mg@NFC/BN and that is governed by a synergistic combination of protonation, electrostatic interaction, and ligand exchange facilitating inner-sphere complexation and enhancing the phosphate removal process.

Protonation:

$$NFC/BN–Mg–OH + H^+ \leftrightarrow NFC/BN–Mg–OH_2^+ \quad (5)$$

Electrostatic interaction:

$$NFC/BN–Mg–OH_2^+ + H_2PO_4^- \leftrightarrow (NFC/BN–Mg–OH_2^+ \cdot H_2PO_4^-) \quad (6)$$

Ligand exchange:

$$(NFC/BN–Mg–OH \cdot H_2PO_4^-) \leftrightarrow NFC/BN–Mg–H_2PO_4 + OH^- \quad (7)$$

$$2(NFC/BN–Mg–OH) + HPO_4^{2-} \leftrightarrow (NFC/BN–Mg)_2–HPO_4 + 2OH^- \quad (8)$$

4 Conclusions

In this study, a magnesium-doped nanofibrillated cellulose/bentonite composite was engineered as a multifunctional adsorbent, providing high-affinity binding sites and structural stability for effective phosphate removal and its reuse in soil water retention. The synergistic interaction among NFC, bentonite, and Mg^{2+} ions played a crucial role in significantly enhancing the adsorption performance, resulting in a maximum phosphate adsorption capacity of 19.2 mg g^{-1}. The adsorption kinetics were best described by the PSO model, indicating that chemisorption governs the process, while the Langmuir isotherm confirmed monolayer adsorption on a homogeneous surface. Thermodynamic analyses revealed that the adsorption process was spontaneous and exothermic in nature. Morphological and spectroscopic characterizations of the phosphate-loaded Mg@NFC/BN composite confirmed successful phosphate immobilization onto the adsorbent surface. The adsorbent maintains effective phosphate removal over repeated cycles, demonstrating excellent regeneration potential and practical applicability. Furthermore, the reclaimed phosphate laden carrier material can be recovered and reused in soil water retention, adding sustainable solutions for water scarcity problems. While the soil water-retention experiments in this study were limited to short-term evaluation, these results provide a basis for further investigations focusing on long-term stability and plant growth performance to fully validate its agronomic applicability. In conclusion, future research may focus on biopolymer–clay hybrid systems with metal-ion functionalization, as they provide a sustainable and versatile material strategy for integrated wastewater remediation, nutrient recovery, and agricultural applications.

Author contributions

All authors contributed to the study conception and design. The first draft of the manuscript was written by Archana Pandey and all authors commented on previous versions of the manuscript. All authors read and approved the final manuscript.

Conflicts of interest

The authors declare no conflict of interest.

Data availability

Data will be made available on request.

Supplementary information (SI) is available. See DOI: https://doi.org/10.1039/d5ra08609d.

Acknowledgements

AP thanks MHRD, Govt. of India for providing financial assistance. Authors acknowledge departmental instrumentation facility, Department of Chemistry, IIT BHU and Central Instrumentation Facility (CIF), IIT BHU, Varanasi for their necessary facilities.

References

1 B. Wang, H. Zhang, Z. Xu, Y. Xu, X. Hu, H. Wang, C. Wang and L. Chen, *Sep. Purif. Technol.*, 2022, **290**, 120894.
2 X. Jiang, M. Ma, Y. Cui, B. Lu, Z. Lin and F. Jiang, *Sep. Purif. Technol.*, 2022, **303**, 128239.
3 R. Diaz, B. Mackey, S. Chadalavada, J. kainthola, P. Heck and R. Goel, *Chemosphere*, 2022, **309**, 136518.
4 J. Qu, W. Peng, M. Wang, K. Cui, J. Zhang, F. Bi, G. Zhang, Q. Hu, Y. Wang and Y. Zhang, *Bioresour. Technol.*, 2024, **407**, 131075.

5 G. Li, B. Zheng, W. Zhang, Q. Liu, M. Li and H. Zhang, *Sustainability*, 2024, **16**, 3836.
6 L. Wang, J. Wang, W. Yan, C. He and Y. Shi, *Chem. Eng. J.*, 2020, **387**, 123305.
7 M. Chen, Y. Liu, J. Pan, Y. Jiang, X. Zou and Y. Wang, *Chem. Eng. J.*, 2024, **502**, 157993.
8 S. Kalia, S. Boufi, A. Celli and S. Kango, *Colloid Polym. Sci.*, 2014, **292**, 5–31.
9 A. Pandey, A. Kalamdhad and Y. Chandra, *Environ. Nanotechnol., Monit. Manage.*, 2023, **20**, 100791.
10 Y. Dong, A. Abbasi, S. Mohammadnejad, M. Nasrollahzadeh, R. Sheibani and M. Otadi, *Int. J. Biol. Macromol.*, 2024, **278**, 134747.
11 A. K. Ilango and Y. Liang, *Water Res.*, 2024, **249**, 120927.
12 S. Kalia, S. Boufi, A. Celli and S. Kango, *Colloid Polym. Sci.*, 2014, **292**, 5–31.
13 M. R. Abukhadra, A. Adlii, A. M. El-Sherbeeny, A. T. Ahmed Soliman and A. E. E. Abd Elgawad, *J. Environ. Manage.*, 2020, **273**, 111130.
14 S. Pandey, *J. Mol. Liq.*, 2017, **241**, 1091–1113.
15 S. Hokkanen, A. Bhatnagar, V. Srivastava, V. Suorsa and M. Sillanpää, *Int. J. Biol. Macromol.*, 2018, **118**, 903–912.
16 Z. Guo, D. Zhang, L. Ma, Q. Dai, R. Yang and R. Ao, *J. Water Process Eng.*, 2025, **71**, 107169.
17 D. Vamvuka, K. Stergiou, E. Sdoukou and A. Stratakis, *J. Environ. Chem. Eng.*, 2024, **12**(1), 111907.
18 M. El Bouraie and A. A. Masoud, *Appl. Clay Sci.*, 2017, **140**, 157–164.
19 A. Pandey, A. S. Kalamdhad and Y. C. Sharma, *Sustainable Chem. Pharm.*, 2024, **37**, 101373.
20 H. El Boujaady, M. Mourabet, M. Bennani-Ziatni and A. Taitai, *J. Assoc. Arab Univ. Basic Appl. Sci.*, 2014, **16**, 64–73.
21 S. Hokkanen, E. Repo and M. Sillanpää, *Chem. Eng. J.*, 2013, **223**, 40–47.
22 M. R. Abukhadra, A. S. Mohamed, A. M. El-Sherbeeny, A. Nadeem and S. F. Ahmad, *Chem. Phys. Lett.*, 2020, **755**, 137818.
23 M. R. Abukhadra, A. Adlii, A. M. El-Sherbeeny, A. T. Ahmed Soliman and A. E. E. Abd Elgawad, *J. Environ. Manage.*, 2020, **273**, 111130.
24 M. K. Singh, R. Pandey, A. Sharma and N. V. C. Rao, *Geosyst. Geoenviron.*, 2022, **1**, 100020.
25 A. Toscan, R. C. Fontana, J. Andreaus, M. Camassola, R. M. Lukasik and A. J. P. Dillon, *Bioresour. Technol.*, 2019, **285**, 121346.
26 A. L. Obsa, N. T. Shibeshi, E. Mulugeta and G. A. Workeneh, *Results Eng.*, 2024, **21**, 101756.
27 W. Li, L. Zhang, T. Su, X. Luo, X. Xie and Z. Qin, *Adv. Compos. Hybrid Mater.*, 2025, **8**, 119.
28 C. Zou, Y. Zhou, Q. Wu, F. Nie and S. Xiang, *J. Solid State Chem.*, 2025, **346**, 125260.
29 R. Li, J. J. Wang, B. Zhou, M. K. Awasthi, A. Ali, Z. Zhang, A. H. Lahori and A. Mahar, *Bioresour. Technol.*, 2016, **215**, 209–214.
30 H. Hajjaoui, A. Soufi, M. Abdennouri, S. Qourzal, H. Tounsadi and N. Barka, *Appl. Surf. Sci. Adv.*, 2022, **9**, 100263.
31 D. Thakre, S. Rayalu, R. Kawade, S. Meshram, J. Subrt and N. Labhsetwar, *J. Hazard. Mater.*, 2010, **180**, 122–130.
32 I. Hongrattanavichit and D. Aht-Ong, *J. Cleaner Prod.*, 2020, **277**, 123471.
33 F. Xie, F. Wu, G. Liu, Y. Mu, C. Feng, H. Wang and J. P. Giesy, *Environ. Sci. Technol.*, 2014, **48**, 582–590.
34 L. Alves, E. Ferraz and J. A. F. Gamelas, *Adv. Colloid Interface Sci.*, 2019, **272**, 101994.
35 A. Etale, A. J. Onyianta, S. R. Turner and S. J. Eichhorn, *Chem. Rev.*, 2023, **123**, 2016–2048.
36 T. Bao, M. M. Damtie, C. yan Wang, Z. Chen, Q. Tao, W. Wei, K. Cho, P. Yuan, R. L. Frost and B. J. Ni, *J. Cleaner Prod.*, 2024, **447**, 141425.
37 Y. Mittal, P. Srivastava, B. C. Tripathy, N. K. Dhal, F. Martinez, N. Kumar and A. K. Yadav, *Chemosphere*, 2023, **349**, 140649.
38 L. guo Yan, K. Yang, R. ran Shan, T. Yan, J. Wei, S. jun Yu, H. qin Yu and B. Du, *J. Colloid Interface Sci.*, 2015, **448**, 508–516.
39 A. Pandey, A. S. Kalamdhad and Y. C. Sharma, *Int. J. Biol. Macromol.*, 2025, **288**, 138743.
40 L. Wang, J. Wang, W. Yan, C. He and Y. Shi, *Chem. Eng. J.*, 2020, **387**, 123305.
41 C. Lee, P. Madhusudan and J. O. Kim, *Sep. Purif. Technol.*, 2024, **330**, 125313.
42 Y. Zhang, X. Wang, Z. qiang Hu, Q. qing Xiao and Y. Wu, *Sep. Purif. Technol.*, 2025, **353**, 128453.
43 A. S. Eltaweil, K. Ibrahim, E. M. Abd El-Monaem, G. M. El-Subruiti and A. M. Omer, *J. Cleaner Prod.*, 2023, **385**, 135640.
44 H. Xi, Q. Li, Y. Yang, J. Zhang, F. Guo, X. Wang, S. Xu and S. Ruan, *Appl. Clay Sci.*, 2021, **201**, 105919.
45 V. T. Trinh, T. M. P. Nguyen, H. T. Van, L. P. Hoang, T. V. Nguyen, L. T. Ha, X. H. Vu, T. T. Pham, T. N. Nguyen, N. V. Quang and X. C. Nguyen, *Sci. Rep.*, 2020, **10**, 1–13.
46 S. Pap, C. Kirk, B. Bremner, M. Turk Sekulic, L. Shearer, S. W. Gibb and M. A. Taggart, *Water Res.*, 2020, **173**, 115573.
47 H. Xi, H. Jiang, D. Zhao, A. H. Zhang, B. Fan, Y. Yang and J. Zhang, *J. Cleaner Prod.*, 2025, **93**(1), 80–111.
48 M. Li, J. Liu, Y. Xu and G. Qian, *Environ. Rev.*, 2016, **24**, 319–332.
49 L. Feng, Q. Zhang, F. Ji, L. Jiang, C. Liu, Q. Shen and Q. Liu, *Chem. Eng. J.*, 2022, **430**, 132754.
50 A. Alhujaily, Y. Mao, J. Zhang, J. Ifthikar, X. Zhang and F. Ma, *J. Taiwan Inst. Chem. Eng.*, 2020, **117**, 75–85.
51 C. Fan and Y. Zhang, *J. Geochem. Explor.*, 2018, **188**, 95–100.
52 K. Skaalsveen, J. Ingram and L. E. Clarke, *Soil Tillage Res.*, 2019, **189**, 98–109.
53 I. Kassem, E. H. Ablouh, F. Z. El Bouchtaoui, H. Hannache, H. Ghalfi, H. Sehaqui and M. El Achaby, *ACS Sustain. Chem. Eng.*, 2022, **10**, 15250–15262.
54 P. Wen, Z. Wu, Y. Han, G. Cravotto, J. Wang and B. C. Ye, *ACS Sustain. Chem. Eng.*, 2017, **5**, 7374–7382.
55 X. Wang, S. Lü, C. Gao, C. Feng, X. Xu, X. Bai, N. Gao, J. Yang, M. Liu and L. Wu, *ACS Sustain. Chem. Eng.*, 2016, **4**, 2068–2079.
56 Q. Hu, Q. Pei, Y. Zhang, S. Pang and C. Feng, *J. Water Process Eng.*, 2024, **66**, 106080.

57 J. Mokrzycki, M. Fedyna, M. Marzec, R. Panek, J. Szerement, L. Marcińska-Mazur, R. Jarosz, T. Bajda, W. Franus and M. Mierzwa-Hersztek, *J. Water Process Eng.*, 2022, **50**, 103299.
58 M. Schindler, F. C. Hawthorne, M. S. Freund and P. C. Burns, *Geochim. Cosmochim. Acta*, 2009, **73**, 2488–2509.
59 M. Chen, Y. Liu, J. Pan, Y. Jiang, X. Zou and Y. Wang, *Chem. Eng. J.*, 2024, **502**, 157993.
60 W. Du, Y. Li, X. Xu, Y. Shang, B. Gao and Q. Yue, *J. Colloid Interface Sci.*, 2019, **533**, 692–699.
61 T. Bao, M. M. Damtie, C. y. Wang, Z. Chen, Q. Tao, W. Wei, K. Cho, P. Yuan, R. L. Frost and B. J. Ni, *J. Cleaner Prod.*, 2024, **447**, 141425.
62 B. Wang, H. Zhang, Z. Xu, Y. Xu, X. Hu, H. Wang, C. Wang and L. Chen, *Sep. Purif. Technol.*, 2022, **290**, 120894.
63 S. Hokkanen, A. Bhatnagar and M. Sillanpää, *Water Res.*, 2016, **91**, 156–173.
64 A. K. Ilango and Y. Liang, *Water Res.*, 2024, **249**, 120927.
65 W. Li, L. Zhang, T. Su, X. Luo, X. Xie and Z. Qin, *Adv. Compos. Hybrid Mater.*, 2025, **8**, 119.
66 L. Alves, E. Ferraz and J. A. F. Gamelas, *Adv. Colloid Interface Sci.*, 2019, **272**, 101994.
67 C. Zou, Y. Zhou, Q. Wu, F. Nie and S. Xiang, *J. Solid State Chem.*, 2025, **346**, 125260.
68 X. Xu, Y. Cheng, X. Wu, P. Fan and R. Song, *Appl. Clay Sci.*, 2020, **190**, 105547.
69 R. Li, J. J. Wang, B. Zhou, M. K. Awasthi, A. Ali, Z. Zhang, A. H. Lahori and A. Mahar, *Bioresour. Technol.*, 2016, **215**, 209–214.